DEVELOPMENT OF EJECTOR CYCLE FOR SOLAR AIR-CONDITIONING SYSTEM POWERED BY STORED THERMAL ENERGY PART 2. CFD ANALYSIS FOR EJECTOR DESIGN

Tatsuya Ito[1], Haruki Sato[2] and Akiko Matsuo[2]

[1] Graduate School of Science and Technology, Keio University, Yokohama (Japan)

[2] Faculty of Science and Technology, Keio University, Yokohama (Japan)

1. Introduction

From the viewpoints of addressing the issue of global warming and depletion of fossil energy resources, utilization of renewable energy, which can reduce CO_2 emission, is important. On the other hand, demands for air-conditioning are increasing in many developing countries. Therefore, an air-conditioning system that works with renewable energy is currently developed. Figure 1 shows the schematic diagram of the ejector refrigeration cycle, which was produced by Chan et al. (2008). This cycle can provide cooling (at evaporator) by using solar thermal energy (at generator) with drastically small consumption of electricity (at pump). Furthermore, this system can utilize lower temperature thermal energy sources such as solar thermal energy, or exhaust heat at low temperature of 60℃. Since the ejector is the main component in this cycle, the design of the ejector is influential to the cycle efficiency.

The schematic structure of the ejector is shown in Fig. 2. This type of ejector has two inflow sections: the driven flow accelerated supersonically inside the converging-diverging nozzle, and the suction flow entrained by the driven flow. They are mixed in the mixing section, which is a straight tube, and the mixed gas flows into the diffuser. In this paper, the response characteristics of the ejector configuration are investigated utilizing computational fluid dynamics (CFD). The principle of the cycle is experimentally confirmed in another report (Part 1).

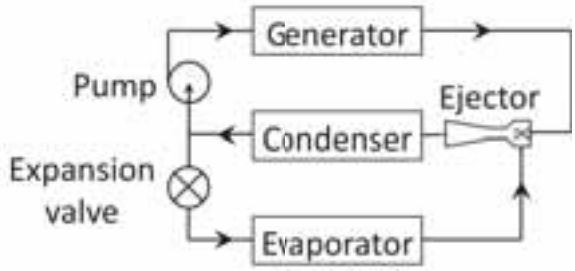

Fig. 1: Schematic diagram of the ejector refrigeration cycle

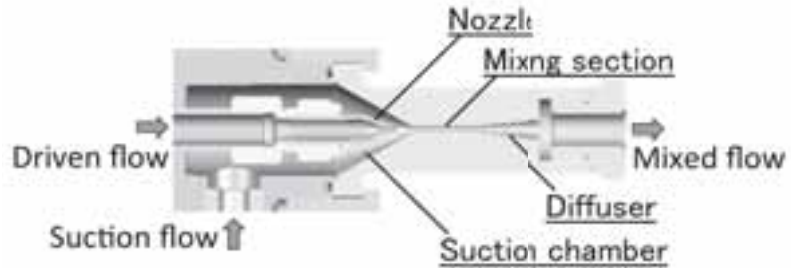

Fig. 2: Schematic structure of the ejector

2. Numerical setup

Chan et al. (2008) reported the preliminary design of the ejector configuration based on the analysis of thermodynamics relations with shock-circle model in the system, but no regards were given about the effect of multi-dimensional compressible working fluid. Hence, aerodynamics in the ejector is analyzed by CFD using the compressible, axisymmetric and two-dimensional Navier-Stokes solver for governing equations.

Since the ejector configuration is fairly axisymmetric, the flow field in the ejector could also be assumed axisymmetric. The numerical scheme used are 3rd order Simple High-resolution Upwind Scheme (SHUS, Shima and Jounouchi, 1995), and 2nd order central difference method for convective and viscous terms respectively. For time integration, Lower-Upper Alternating Direction Implicit (LU-ADI) factorization method (Obayashi and Kuwahara, 1986, and Obayashi et al. (1986)) is adopted. To estimate the flow field of turbulent boundary layers, Baldwin-Lomax turbulence model (Baldwin and Lomax, 1978) is also adopted.

Equation 1 shows the relation between coefficient of performance (COP) and entrainment ratio ω, where Δh stands for the change in specific enthalpy, and subscript 'e' and 'g' each stand for evaporator and generator. Furthermore, the entrainment ratio, which is defined as mass flow rate of the suction flow (subscript 's') divided by that of the driven flow (subscript 'd'), is shown in Eq. 2. Changes in specific enthalpy Δh in Eq. 1 are nearly constant. Because of this, the entrainment ratio is approximately proportional to the COP. Therefore the entrainment ratio is used as a cycle efficiency evaluation indicator. Since the driven flow is always choked at converging-diverging nozzle in this condition, the entrainment ratio is proportional to the mass flow rate of the suction flow.

As the parameter in calculations, backpressure p_b (condensing pressure), nozzle position d (distance from nozzle exit to mixing section entrance), and mixing section length L and its cross-section area A were used. Table 1 shows experimental measurement values, and these values are used as boundary conditions for numerical calculation. Computational grid, boundary conditions and four parameters in calculations are shown in Fig. 3. Total number of nodes sum up to approximately quarter-million, and the grid spacing near the outer wall is dense for conducting viscous calculation. Computational grid is adjusted corresponding to parameters d, L and A. The working fluid in the ejector refrigeration cycle is HFC-134a (CH_2F-CF_3), with constant specific heat ratio $\gamma = 1.119$.

$$\mathrm{COP} = \omega \frac{\Delta h_e}{\Delta h_g} \qquad \text{(eq. 1)}$$

$$\omega = \frac{\dot{m}_s}{\dot{m}_d} \qquad \text{(eq. 2)}$$

Tab. 1: Experimental measurement and reference numerical values at ejector boundaries

	Driven flow (Generator)	Suction flow (Evaporator)	Mixed flow (Condenser)
Pressure [MPa]	1.690	0.483	0.718
Temperature [K]	329.8	295.8	308.1

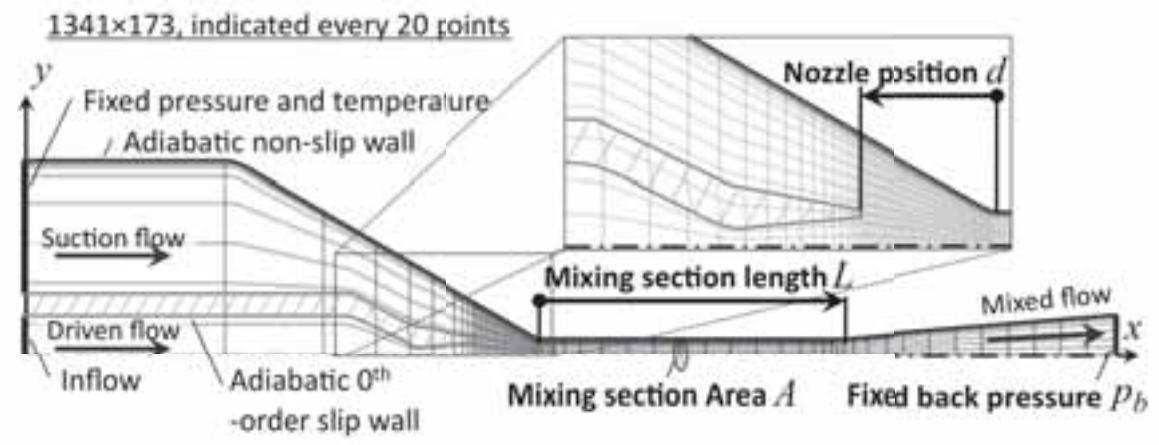

Fig. 3: Computational grid, boundary conditions and parameters in calculations (bold)

3. Results and discussions

3.1. Response characteristics of backpressure

Figure 4 shows the relation between the entrainment ratio ω and the backpressure p_b in experimental and numerical results at the nozzle position d = 5 mm, the mixing section length L/L_0 = 1.0 and its cross-section area A/A_0 = 1.0 (L_0 = 23.0 mm and A_0 = 4.37 mm^2, obtained by Chan et al. (2008) as the optimized value). In both results, the entrainment ratio begins to decrease at approximately 0.71 MPa (critical backpressure, $p_{b,crit}$), which is significant to predict the ejector performance. The simulated entrainment ratio at $p_b < p_{b,crit}$ is constant, approximately ω = 0.285. Therefore, its behavior implies that double choking (critical mode) must occur in the driven flow and the mixed flow concurrently. However, the entrainment ratio at $p_b > p_{b,crit}$ decrease responding to increment of backpressure (subcritical mode). Therefore double choking (critical mode) could be confirmed by the unchanged entrainment ratio at lower backpressure condition. The ejector refrigeration cycle should be operated on critical mode for the backpressure robustness.

Figure 5 shows the pressure distributions at the central axis of the mixing section and the diffuser in each backpressure conditions from 0.40 to 0.75 MPa. The pressure distributions were nondimensionalized by the stagnation driven pressure p_0 = 1.69 MPa. The x origin is the entrance of the mixing section, and the backpressure is fixed at the exit of the diffuser, x = 45 mm. On critical mode (when p_b = 0.40, 0.55 and 0.70 MPa in this conditions), pressure distributions in mixing section are completely identical. From this fact, choking in the mixing section is confirmed. Moreover, a shock wave stands in the diffuser, and moves downstream depending on the descent of the backpressure. On the other hand, on subcritical mode (when p_b = 0.718 and 0.75 MPa), pressure distribution in the mixing section rise due to increment of backpressure.

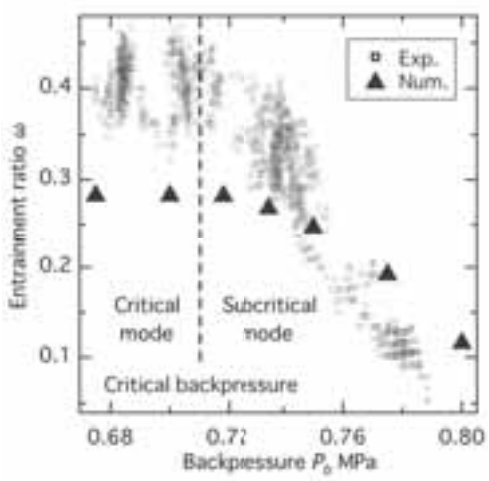

Fig. 4: Entrainment ratio vs. backpressure

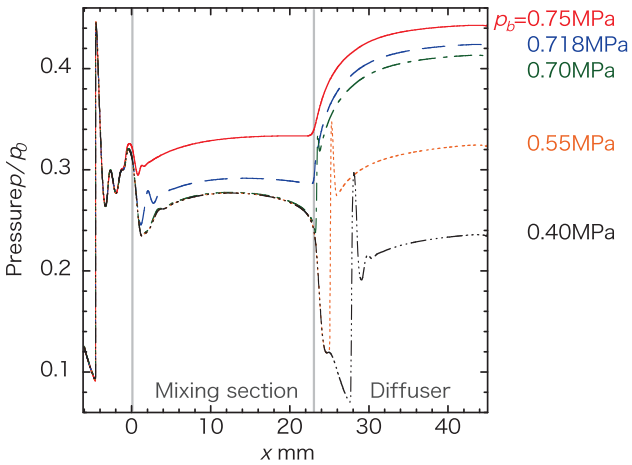

Fig. 5: Pressure distribution at the central axis in each backpressure when d = 5.0 mm (backpressure is fixed at x = 45 mm)

3.2. Response characteristics of nozzle position and mixing section length

Figure 6 shows the entrainment ratio in the case of the nozzle position d = 1, 2, 3, 4 and 5 mm, mixing section length L/L_0 = 0.5, 1.0 and 1.5, at the mixing section area A/A_0 = 1.0 and p_b = 0.718 MPa. It was confirmed that L/L_0 = 1.0 achieved the best performance in each nozzle position. Therefore the mixing section length L/L_0 discussed below is fixed at 1.0. For instance, the entrainment ratio at d = 2 mm is about 8% higher than that at d = 5 mm. The conditions d = 1, 2, 3 and 4 mm (without 5 mm) are operated on critical mode. The reason that the entrainment ratios on critical mode are different in spite of the choking phenomenon seems to be differences of effective cross-section area, which varies depending on the displacement thickness of boundary layer.

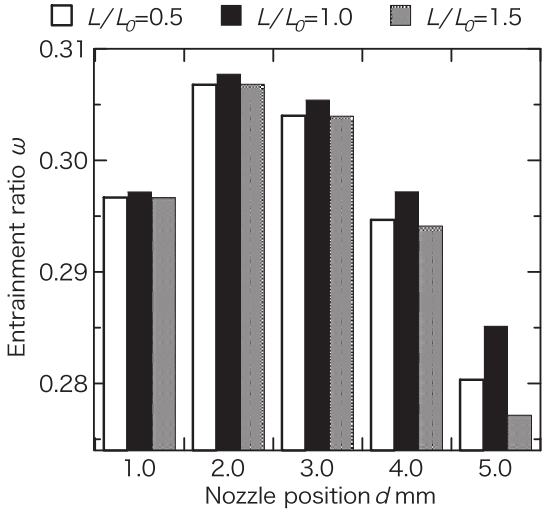

Fig. 6: Entrainment ratio vs. nozzle position and mixing section length at p_b = 0.718 MPa

3.3. Response characteristics of mixing section area

Figure 7 shows the response characteristics of the mixing section area A/A_0 from 1.0 to 2.0 at p_b = 0.718 MPa and d = 2 mm. There is an entrainment ratio peak in Fig. 7. The entrainment ratio monotonically increases within the range from 1.0 to 1.6 in the mixing section area. The efficiency at A/A_0 = 1.6 is more than twice as high as that at A/A_0 = 1.0, which is conventional configuration, and increases about 112%. Conversely, The entrainment ratio monotonically decreases after the peak, A/A_0 > 1.6. Moreover, below the A/A_0 = 1.4, it was confirmed that double choking occurs, and the entrainment ratio increases linearly. Therefore, A/A_0 = 1.4 can be estimated as the critical point characterized by mixing flow choking.

Figure 8 shows the relation between the entrainment ratio and the backpressure in each mixing section area A/A_0 = 1.0, 1.2, 1.4 and 1.6 at d = 2 mm. Entrainment ratios on critical mode increase linearly with the mixing section area A/A_0, as shown in Fig. 7. However, critical backpressures decrease almost linearly with A/A_0. Therefore, the backpressure must be lowered for operation on critical mode. Furthermore, the performance degradation on subcritical mode steepens by enlargement of the mixing section area.

Figure 9 shows the relation between the entrainment ratio and the mixing section area in each backpressure at d = 2 mm. Figure 9 is plotted by the same data of Fig. 8, and another aspect of the response characteristics. In the case of larger mixing section area, entrainment ratios decrease rapidly responding to increment of backpressure. On the other hand, the case when mixing section area is smaller still remains on critical mode in spite of the high backpressure. From these facts, the optimum mixing section area decreases in size responding to increment of backpressure. Therefore, the designing mixing section area depends on the backpressure variation range.

Figure 10 shows pressure and Mach number distributions around the mixing section in each mixing section area A/A_0 = 1.0, 1.2, 1.4 and 1.6 at p_b = 0.675 MPa (critical mode), and d = 2 mm. The inner wall between the two inflow sections is colored gray. Pressure and Mach number distributions are respectively shown above and below the central axis. Driven flows are choked at each condition, and shock structures at nozzle exit are completely identical. In addition another shock wave stands at the mixing section or at the diffuser,

responding to the conditions. Mach number in the mixing section increases due to increment of the mixing section area A/A_0. Since Mach number in the suction chamber nearly equals zero, the configuration of suction chamber plays only a minor role in the ejector performance.

Figure 11 shows the pressure distributions at the central axis of the mixing section and the diffuser at the same conditions shown in Fig. 10. The stagnation driven pressure p_0 and the x-axis are same as Fig. 5. On critical mode, pressure upstream of the shock at the mixing section decreases responding to increment of the mixing section area A/A_0. This is because, when the mixing section area becomes large, the entrainment ratio increase, which means the increase of mixture proportion of the suction flow. The stagnation pressure of the suction flow is lower than that of the driven flow; it makes the mixture pressure lower. Furthermore, the weak shock moves upstream depending on increment of the mixing section area.

Figure 12 shows the relation between the entrainment ratio and the nozzle position in the critical mode (p_b = 0.650 MPa) and subcritical mode (p_b = 0.718 MPa) at A/A_0 = 1.6. On subcritical mode, the entrainment ratio becomes higher as the nozzle position d decrease. However, on critical mode, the entrainment ratio decreases with increment of nozzle position at $d \leq 2$ mm. Moreover, in the case that the nozzle position is larger than 2 mm, the entrainment ratios becomes constant, and the same tendency of the response characteristics of nozzle position on critical mode is denoted by Rusly et al. (2005). It is also revealed that the tendency on subcritical mode is obviously different from that on critical mode.

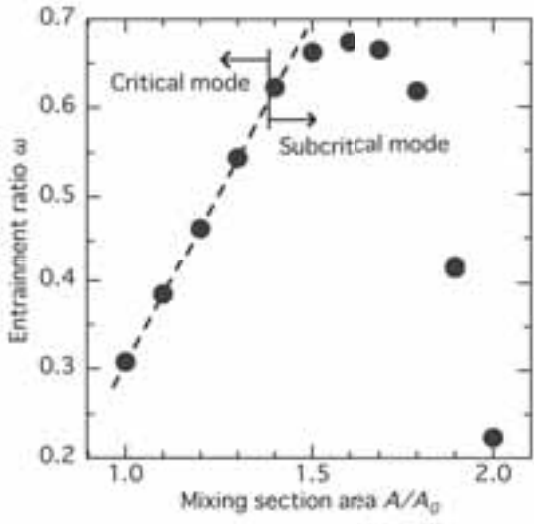

Fig. 7: Entrainment ratio vs. mixing section area at p_b = 0.718 MPa, and d = 2.0 mm

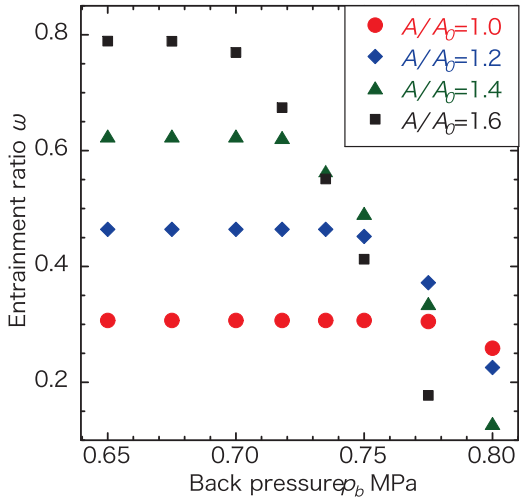

Fig. 8: Entrainment ratio vs. backpressure in each mixing section area at d = 2.0 mm

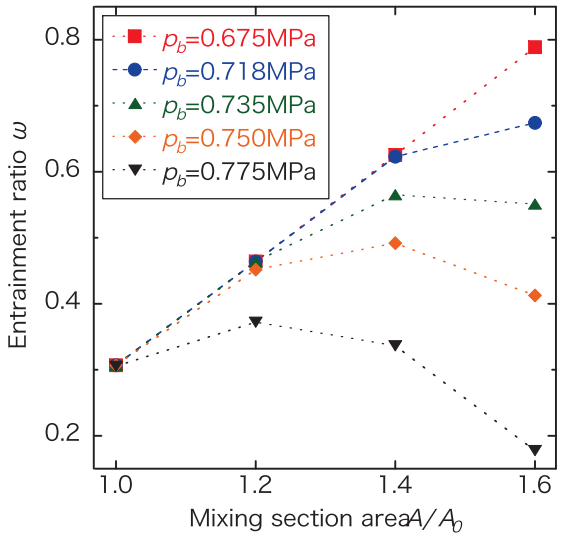

Fig. 9: Entrainment ratio vs. mixing section area in each backpressure at d = 2.0 mm

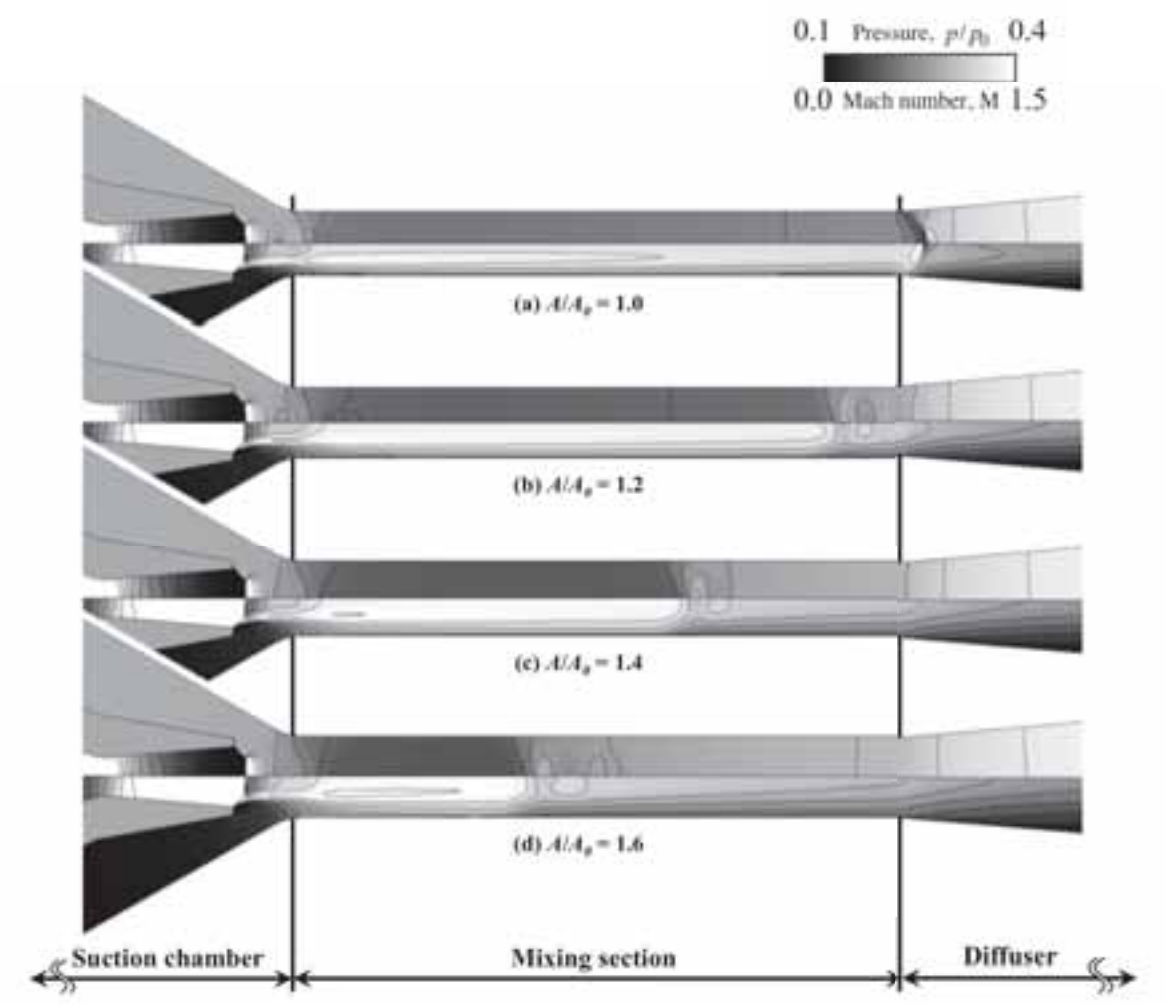

Fig. 10: Pressure and Mach number distributions around the mixing section at p_b = 0.675 MPa (critical mode), and d = 2 mm

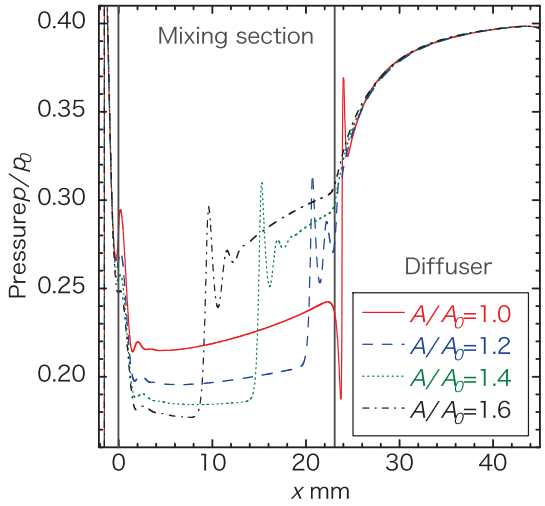

Fig. 11: Pressure distribution in mixing section and diffuser at p_b = 0.675 MPa (critical mode), and d = 2.0 mm

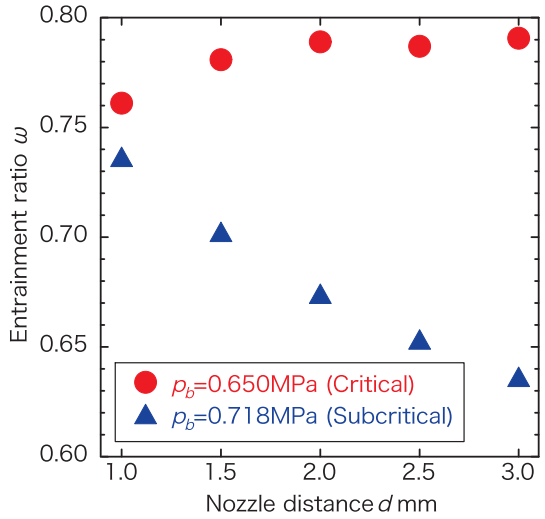

Fig. 12: Entrainment ratio vs. nozzle position in critical and subcritical mode at A/A_0 = 1.6, and d = 2.0 mm

4. Conclusions

The response characteristics of the ejector configuration were investigated using computational fluid dynamics (CFD) code of the compressible, axisymmetric and two-dimensional Navier-Stokes solver for governing equations. This simulation method was validated based on the comparison with the experimental critical backpressure.

It was confirmed that L/L_0 = 1.0 (L_0 = 23.0 mm, obtained by Chan et al. (2008) as the optimized value) achieved the best performance in each nozzle position. However, the mixing section length has an insignificant effect on the ejector performance. On critical mode, where double choking at the nozzle throat and at the mixing section occur, it was confirmed that pressure distributions upstream of the shock at the mixing section were completely identical. In the response characteristics of the mixing section area, there is an entrainment ratio peak at A/A_0 = 1.6 (A_0 = 4.37 mm^2) when p_b = 0.718 MPa. The efficiency at A/A_0 = 1.6 is about 112% higher than that at A/A_0 = 1.0. Entrainment ratios on critical mode increase linearly responding to increment of the mixing section area. On the other hand, the critical backpressure decreases almost linearly with increment of the mixing section area. Therefore, the optimum mixing section area decreases in size responding to increment of backpressure. Furthermore, the tendency of the response characteristics of the nozzle position is widely different by operating (critical or subcritical) mode.

5. Acknowledgement

This work was supported in part by Grant in Aid for the Global Center of Excellence Program “Center for Education and Research of Symbiotic, Safe and Secure System Design” from the Ministry of Education, Culture, Sport, and Technology in Japan. This work was also partially supported by the Research Grant of Keio Leading-edge Laboratory (KLL) of Science and Technology.

6. References

Baldwin, B.S. and Lomax, H., 1978. Thin-layer approximation and algebraic model for separated turbulent flows. AIAA Paper, 78, 257

Chan, S., Sato, H., Suwono, A., Astina, I M., Darmanto, P. S., 2008. Ejector-based refrigeration cycle using HCs as the working fluid. 8th IIR Gustav Lorentzen Conference on Natural Working Fluids, Copenhagen.

Obayashi, S. and Kuwahara, K., 1986. An approximate LU factorization method for the compressive Navier-Stokes equations. J. Comput. Phys. 63, 157-167

Obayashi, S., Matsushima, K., Fujii, K. and Kuwahara, K., 1986. Improvements in efficiency and reliability for Navier-Stokes computations using the LU-ADI factorization algorithm. AIAA Paper, 86, 338

Rusly, E., Aye, L., Charters, W.W.S., and Ooi, A., 2005. CFD analysis of ejector in a combined ejector cooling system. J. of Refrig. 28, 1092-1101

Shima, E. and Jounouchi, T., 1995. Role of computational fluid dynamics in aeronautical engineering (No. 12) -Formulation and verification of uni-particle upwind schemes fort the Euler equations-. Proceedings of the 12th NAL Symposium on Aircraft Computational Aerodynamics, Japan, 255-260 [Written in Japanese]